

# Shock and Static Pressure Demagnetization of Pyrrhotite and Implications for the Martian Crust

## - Supplemental material -

Karin L. Louzada<sup>1\*</sup>, Sarah T. Stewart<sup>1</sup>, Benjamin P. Weiss<sup>2</sup>, Jérôme Gattacceca<sup>3</sup>, Natalia S.  
Bezaeva<sup>4</sup>

<sup>1</sup>Department of Earth and Planetary Sciences, Harvard University, 20 Oxford Street, Cambridge, MA 02138, USA

<sup>2</sup>Department of Earth, Atmospheric and Planetary Sciences, Massachusetts Institute of Technology 54-814, 77 Massachusetts Avenue, Cambridge, MA 02139, USA

<sup>3</sup>Department of Geophysics and Planetology, CEREGE (CNRS, Aix-Marseille University), BP 80, 13545 Aix en Provence Cedex 4, France

<sup>4</sup>Earth Physics Department, Faculty of Physics, M.V. Lomonosov Moscow State University, Leninskie gory, 119991, Moscow, Russia

\*louzada@post.harvard.edu

### Contents:

	<i>Figure</i>	<i>Table</i>	<i>page</i>
1. Low-temperature cycling	Figure S1		2
2. X-ray diffraction	Figure S2	Table S1	3
3. Chemical composition		Table S2	5
4. Magnetic hysteresis		Table S3	6
5. Anisotropy of magnetic susceptibility	Figure S3	Table S4	8
6. Pressure distribution in the shocked samples	Figure S4		10
7. Impedance match solution		Table S5	11
8. Hugoniot Elastic Limit	Figure S5	Table S6	12
9. Photomicrographs of shocked pyrrhotite	Figure S6		14
10. Domain interactions	Figure S7		15
11. Magnetic imaging of pyrrhotite nodule	Figure S8		17
12. References			18

*Submitted to EPSL - July 10, 2009*

## 1. Low-temperature cycling

Low-temperature cycling of pyrrhotite (Figure S1) samples was performed on a Quantum Devices DC Magnetic Properties Measurement System at the Center for Material Sciences and Engineering at MIT. Specimens were saturated in a 1.5-2 T field. After quenching of the magnet, the temperature was slowly decreased to 4K and then increased to room temperature. Open loops, with a small recovery ('y' in inset in Figure S1D), are indicative of MD fractions (Dekkers et al., 1989). A slight increase in moment below the 30K transition is indicative of superparamagnetic fractions (Rochette et al., 1990). Both the fraction of remanence remaining at 4K and the fraction of remanence recovered upon cycling through the 30K transition increase as a result of shock (Figures S1C and D), indicative of an effective decrease in grain size. At 30K the spontaneous magnetization in monoclinic pyrrhotite rotates away from the basal plane and towards the pseudo-hexagonal *c*-axis of pyrrhotite.

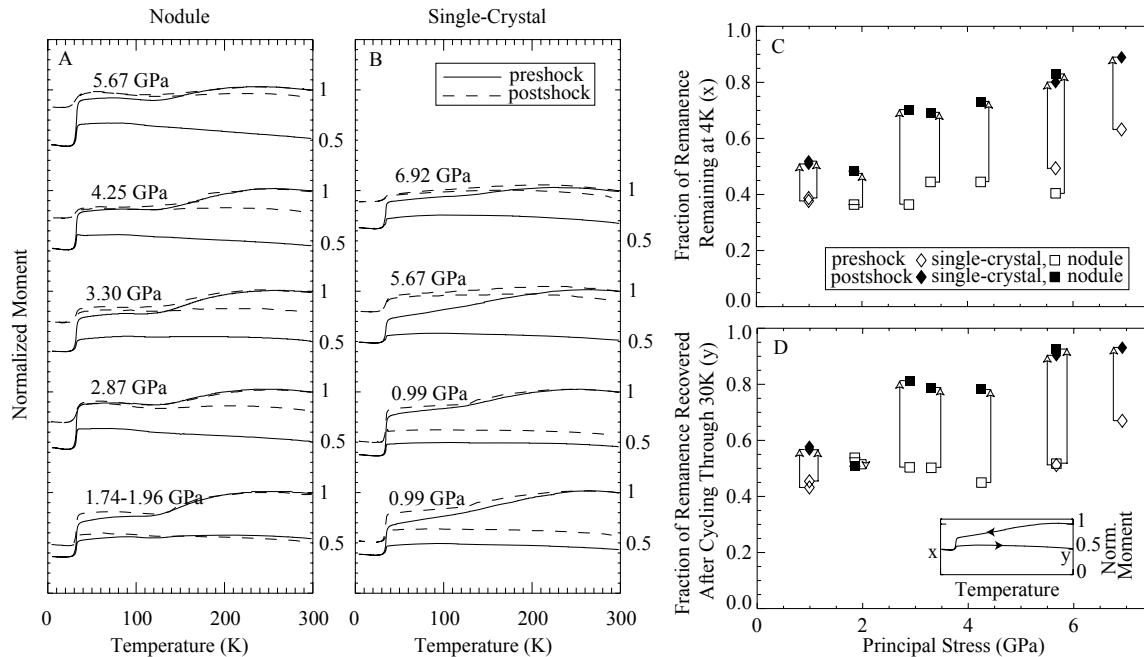


**Figure S1** Low-temperature cycling of pre-shock (solid) and post-shock (dashed) pyrrhotite (A) nodule (No. 98080) and (B) single-crystal (No. 127037) specimens. Changes in the low-temperature memory: (C) fraction of remanence remaining at 4K ('x' in inset) and (D) fraction of remanence recovered after cycling through the 30K transition ('y' in inset) versus principal stress in the shock samples. Open symbols denote pre-shock values, solid symbols – post-shock values.

## 2. X-ray diffraction

X-ray diffraction patterns were obtained for powdered samples using the Scintag XDS2000 fixed sample position powder diffractometer between 2 and 70° (2 $\theta$ ) at Harvard University. D-spacing values of peaks identified with known indices of pyrrhotite are shown in Table S1. Two additional weak peaks were detected at 2.8483 – 2.8643 Å and 1.5968 – 1.6096 Å, respectively. The latter peak could be related to the (312) plane in chalcopyrite (CuFeS<sub>2</sub>), which may occur as small inclusions in natural pyrrhotite. Note that Cu was not measured in the microprobe analyses (Table S2) and this interpretation cannot be independently confirmed. Lattice parameters,  $a$  and  $c$ , were determined for a hexagonal lattice using the technique described in Nkoma and Ekosse (1999) and are consistent with previous pyrrhotite measurements (Dekkers, 1988; Nkoma and Ekosse, 1999). Thanks to W. Croft, Harvard University.

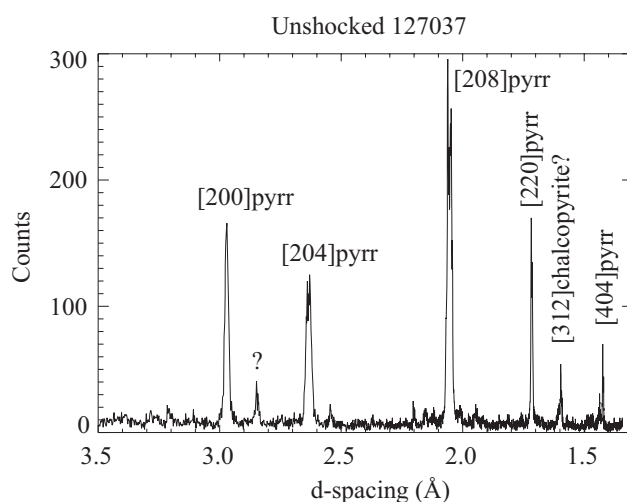


**Figure S2** Example X-ray diffraction pattern for unshocked single-crystal pyrrhotite.

**Table S1** X-ray diffraction results

<i>d</i> -spacing	<i>Unshocked</i>	
	<i>Nodule (No. 98080)</i>	<i>Single-crystal (No. 127037)</i>
$d_{(200)}$ (Å)	2.9737 (0.0058) <sup>a</sup>	2.9703
$d_{(204)}$ (Å)	2.6421 (0.0025) <sup>a</sup>	2.6300
$d_{(208)}$ (Å)	2.0642 (0.0025) <sup>a</sup>	2.0615, 2.0473 <sup>c</sup>
$d_{(220)}$ (Å)	1.7184 (0.0021) <sup>a</sup>	1.7179
$d_{(404)}$ (Å)	1.4324 (0.0005) <sup>b</sup>	1.4238
<i>a</i> (Å)	6.875 (0.006)	6.846 (0.033)
<i>c</i> (Å)	22.89 (0.06)	22.84 (0.23)
	<i>Postshock</i>	
	<i>Nodule (98080-1D)</i>	<i>Single-crystal (127037-A)</i>
	<i>(5.67 GPa)</i>	<i>(6.92 GPa)</i>
$d_{(200)}$ (Å)	2.9839	2.9800
$d_{(204)}$ (Å)	2.6436	2.6436
$d_{(208)}$ (Å)	2.0669	2.0669
$d_{(220)}$ (Å)	1.7215	1.7227
$d_{(404)}$ (Å)	1.4304	
<i>a</i> (Å)	6.874 (0.028)	6.884 (0.005)
<i>c</i> (Å)	22.94 (0.12)	22.91 (0.06)

<sup>a,b</sup> Average of three <sup>(a)</sup>, two <sup>(b)</sup> measurements. <sup>c</sup> Split peak. 1 $\sigma$  errors are indicated in parentheses.

### 3. Chemical composition

Spot microprobe chemical composition analyses were performed using the Camica Electron Microprobe at Harvard University. Operating conditions were 15keV and 30.17 nA, with a beam size of 8  $\mu\text{m}$ . Thanks to David Lange, Harvard University.

**Table S2** Averaged ( $1\sigma$ ) atom percentage chemical composition of pyrrhotite samples

<i>Element</i>	<i>Nodule (No. 98080)</i>	<i>Single-crystal (No. 127037)</i>
S	52.70 (0.34)	53.29 (0.18)
Fe	47.07 (0.23)	46.70 (0.17)
Mn	b.d.l.	b.d.l.
Co	0.056 (0.007)	0.022 (0.005)
Ni	0.226 (0.050)	b.d.l.
Zn	b.d.l.	b.d.l.
total	100.13	100.17
Fe/S	0.893 (0.01)	0.876 (0.01)

b.d.l. = below detection limit

#### **4. Magnetic hysteresis**

Unshocked pyrrhotite magnetic hysteresis measurements (Table S3) were performed on the Micromag Vibrating Sample Magnetometer with  $\pm 1$  T maximum field at CEREGE, France. Postshock pyrrhotite magnetic hysteresis measurements were performed on the Mircromag Vibrating Sample Magnetometer at the Institute for Rock Magnetism, UMN with maximum field  $\pm 1.8$  T. Due to variable monoclinic to hexagonal pyrrhotite distributions in the samples (and the small sample masses) direct comparison of the saturation moment ( $M_s$ ) and saturation remanence ( $M_{rs}$ ) cannot be made between the unshocked and shocked samples in this table,  $M_{rs}/M_s$  comparisons are permitted however. Thanks to M. Jackson and J. Bowles at IRM, UMN.

**Table S3** Magnetic hysteresis results

<i>Hysteresis</i>		<i>Unshocked</i>						
<i>Parameter</i> ( $1\sigma$ )	<i>Nodule (No. 98080)</i> <sup>a</sup>	<i>Single-crystal (No. 127037)</i> <sup>a</sup>		<i>Schist</i> <sup>b</sup>				
$M_s$ ( $\text{Am}^2/\text{kg}$ )	$1.130 (0.027) \times 10^{-3}$	$1.405 (0.029) \times 10^{-2}$		$9.14 (6.02) \times 10^{-2}$				
$M_{rs}$ ( $\text{Am}^2/\text{kg}$ )	$5.644 (0.022) \times 10^{-4}$	$2.089 (0.022) \times 10^{-3}$		$4.48 (2.90) \times 10^{-2}$				
$M_{rs}/M_s$	0.4991 (0.010)	0.1487 (0.004)		0.499 (0.028)				
$B_c$ (mT)	5.507 (0.449)	4.643 (0.028)		23.8 (5.9)				
$B_{cr}$ (mT)	5.481 (0.552)	7.001 (0.075)		31.3 (11.7)				
$B_{cr}/B_c$	0.9941 (0.0224)	1.508 (0.012)		1.29 (0.12)				
mass (mg)	9.7	11.2		173.2-364.7 (n=10)				
Domain size	SD/SP	MD		PSD				
<i>Postshock</i> <sup>c</sup>								
<i>Parameter</i> (RMSres/RMSdata)	<i>Nodule</i>			<i>Single-crystal</i>				
	<i>98080-1L</i> (1.74 GPa)	<i>98080-1K</i> (2.81 GPa)	<i>98080-1H</i> (2.89 GPa)	<i>98080-1A</i> (3.3 GPa)	<i>127037-G</i> (0.99 GPa)	<i>127037-D</i> (5.67 GPa)	<i>127037-L</i> <sup>d</sup> (9.83 GPa)	<i>127037-N*</i> (9.83 GPa)
$M_s$ ( $\times 10^{-3} \text{Am}^2/\text{kg}$ )	0.705 (0.02)	1.415 (0.07)	2.777 (0.86)	0.9217 (0.06)	1.065 (0.12)	4.329 (0.39)		15.95 (0.79)
$M_{rs}$ ( $\times 10^{-3} \text{Am}^2/\text{kg}$ )	0.374 (0.03)	0.720 (0.06)	1.186 (0.30)	0.4538 (0.05)	0.330 (0.04)	2.022 (0.22)		7.698 (0.54)
$M_{rs}/M_s$	0.454 (0.06)	0.4266 (0.05)	0.4634 (0.15)	0.4412 (0.07)	0.317 (0.08)	0.4635 (0.04)	0.5527 (0.10)	0.4722 (0.02)
$B_c$ (mT)	8.816 (2.03)	18.37 (2.76)	15.26 (8.70)	9.739 (2.82)		24.08 (10.59)	18.65 (7.65)	46.11 (5.53)
mass (mg)	1.2	12.0	17.3	1.9	1.3	9.2	<0.6	1.8

$M_s$  = in field saturation magnetization (corrected for paramagnetic contribution),  $M_{rs}$  = saturation remanence,  $B_c$  = coercivity,  $B_{cr}$  = coercivity of remanence.

<sup>a</sup> Average hysteresis parameters ( $1\sigma$ ) of measurements made in three perpendicular orientations. <sup>b</sup> Hysteresis parameters reported in Gattacceca, et al. (2007). <sup>c</sup>

Geometric mean ( $\sqrt[3]{\kappa_1 \cdot \kappa_2 \cdot \kappa_3}$ ) of ellipsoids fit to the hysteresis parameters measured in 12 orientations, where  $\kappa_1$ ,  $\kappa_2$  and  $\kappa_3$  are the principal axes of the ellipsoid. <sup>d</sup> Uncertain mass. \* Shock direction is parallel to the easy plane of magnetization.

## 5. Anisotropy of magnetic susceptibility

The anisotropy of magnetic susceptibility (AMS) of pure pyrrhotite is field dependent (e.g., Martín-Hernández et al., 2008) and measurements using a Geofyzika KLY-2 KappaBridge AC Susceptibility Bridge with A.C. fields of 300 A/m at 920 Hz yielded erroneous results. Therefore, AMS was determined from 27 hysteresis loops in 12 directions obtained on the Princeton Measurements Vibrating Sample Magnetometer at the Institute for Rock Magnetism, UMN, with maximum field  $\pm 1.8$  T. Low field susceptibility was determined from linear slopes fit to the data between -2.5 and +2.5 mT and solved for the susceptibility ellipsoid using the method described in Jelínek (1973) and Coe (1966).

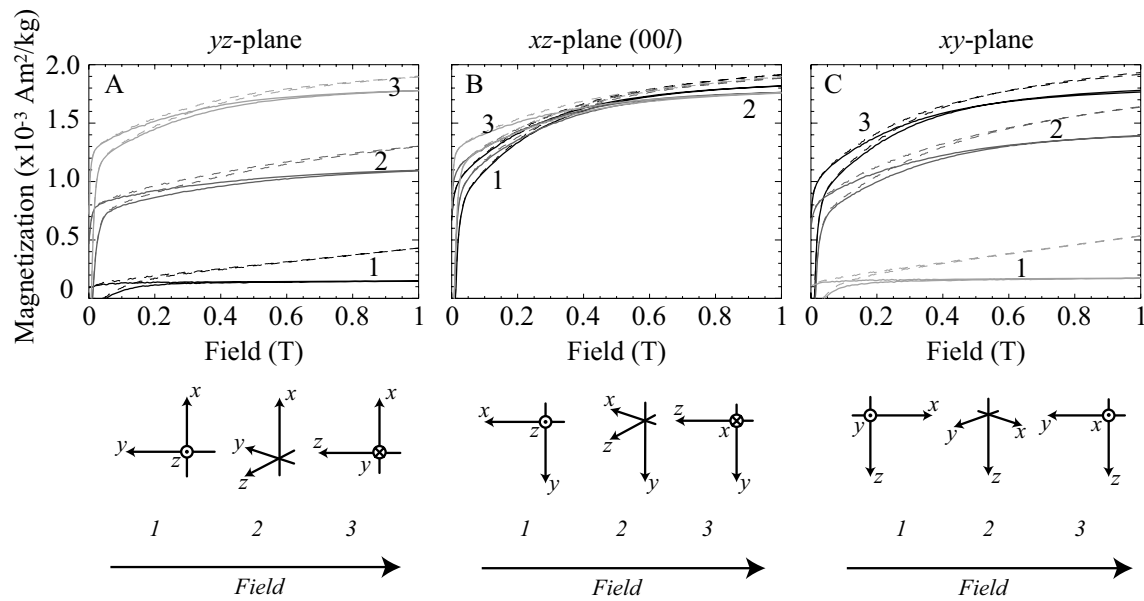


**Figure S3** Partial hysteresis loops for the unshocked single-crystal (No. 127037) in three different orientations (1, 2 and 3). The inducing field is always oriented to the right and is confined to the yz-, xz- and xy-plane of the sample in panels **A**, **B** and **C**, respectively. (Right-handed coordinate system.) The xz-plane is parallel to the (00l) basal-plane. The oblate shape of the anisotropy is evident from the hysteresis loops in the xz-plane. Dashed lines are raw loops, solid lines are loops corrected for paramagnetic signal (linear fit between 1.5 and 1.6 T).

**Table S4** Magnetic anisotropy results

<i>AMS</i>	<i>Unshocked</i>							
	<i>Nodule (No. 98080)</i>			<i>Single-crystal (No. 127037)</i>			<i>Schist<sup>a</sup></i>	
P	45.98			56.24			1.741	
L	29.97			2.202			1.087	
F	1.534			25.53			1.601	
P'	66.37			71.58			1.819	
T	-0.776			0.608			0.697	
RMS(res)/RMS(data)	0.25			0.03				
	<i>Postshock</i>							
	<i>Nodule</i>			<i>Single-crystal</i>				
	<i>98080-1L<sup>a</sup></i>	<i>98080-1K</i>	<i>98080-1H</i>	<i>98080-1A</i>	<i>127037-G</i>	<i>127037-D</i>	<i>127037-L</i>	<i>127037-N*</i>
	<i>(1.74 GPa)</i>	<i>(2.81 GPa)</i>	<i>(2.89 GPa)</i>	<i>(3.3 GPa)</i>	<i>(0.99 GPa)</i>	<i>(5.67 GPa)</i>	<i>(9.83 GPa)</i>	<i>(9.83 GPa)</i>
P	21.96	22.79	5.448	46.46	64.38	253.9	14.20	60.62
L	17.12	4.684	2.410	5.285	1.505	1.375	8.626	1.181
F	1.211	4.865	2.260	8.791	42.77	1984.5	1.646	51.36
P'	31.87	22.79	5.450	46.98	98.62	501.5	16.78	104.2
T	-0.8757	0.0120	-0.0380	0.1325	0.803	0.884	-0.624	0.918
RMS(res)/RMS(data)	0.09	0.11	0.16	0.11	0.07	0.02	0.33	0.08

P = anisotropy degree ( $\kappa_1/\kappa_3$ ), L = lineation ( $\kappa_1/\kappa_2$ ), F = foliation ( $\kappa_2/\kappa_3$ ), P' = corrected anisotropy degree ( $P' = \exp\sqrt{2[(\eta_1-\eta)^2+(\eta_2-\eta)^2+(\eta_3-\eta)^2]}$ ), where  $\eta_i = \ln(\kappa_i)$  and  $\eta = (\eta_1+\eta_2+\eta_3)/3$ , T = shape factor ( $T = (2\eta_2-\eta_1-\eta_3)/(\eta_1-\eta_3)$ ). For a discussion on anisotropy see Jelínek (1981). <sup>a</sup> Measurement performed on the Geofyzika KLY-2 KappaBridge AC Susceptibility Bridge with A.C. field of 300 A/m and 920 Hz by M. Jackson and J. Bowles at IRM, UMN. \* Shock direction is parallel to the easy plane of magnetization. <sup>b</sup> Susceptibility from low-field ( $\pm 3$  mT)

## 6. Pressure distribution in the samples

CTH (McGlaun et al., 1990) simulations of the shock experiments on pyrrhotite indicate that 74 and 94 vol% of the specimen experiences the maximum pressure within 0.5 GPa (13%) and 1.5 GPa (38%), respectively.

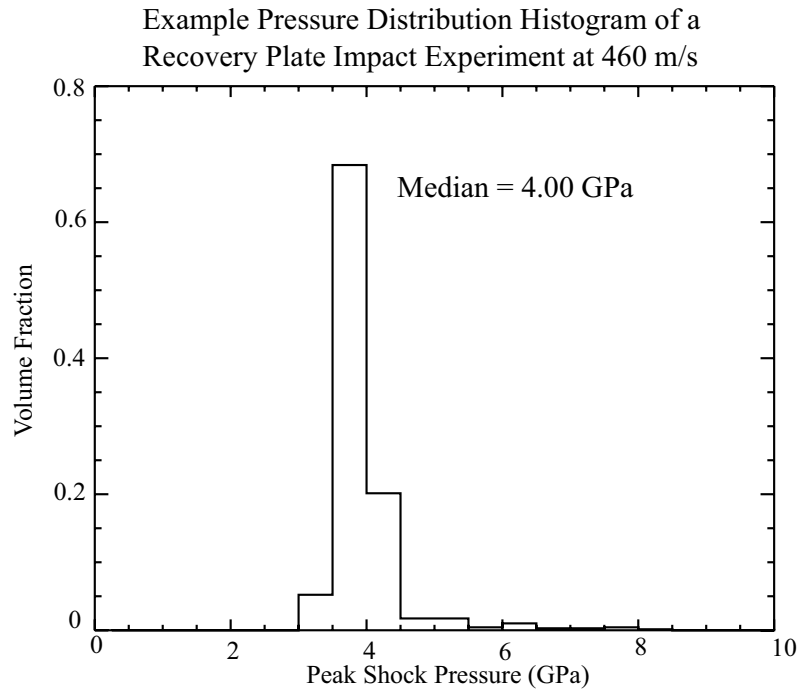


**Figure S4** Histogram of the simulated pressure distribution as a function of sample volume in a pyrrhotite specimen at 460 m/s.

## 7. Impedance match solution

Principal stress in the shock experiments is determined using the impedance match solution, or planar impact approximation (e.g. Boslough and Asay, 1993; Melosh, 1989 p. 54-57), and the material shock parameters in Table II.5. In the impedance match solution the impact is assumed to be between two infinite plates, reducing the problem to one dimension. At impact, the pressure in both the projectile (aluminum) and the target (specimen) must equal. Particle velocity and pressure (principal stress) are related to each other by the Hugoniot equation:

$\sigma_1 = P_0 + \rho_0 U_s u_p$ , where  $\sigma_1$  is principal stress,  $P_0$  is the initial pressure ( $\sim 0$ ),  $\rho_0$  is the initial uncompressed density, and  $U_s$  and  $u_p$  are the shock and particle velocities in km/s, respectively.  $U_s$  and  $u_p$  are related to each other via the empirical relationship:

$U_s = C + s \cdot u_p$ , where  $C$  is the material specific bulk sound speed in km/s and  $s$  is the material specific dimensionless slope (Table S5). The planar impact approximation neglects attenuation of the shock wave and rarefactions that travel inward from the sides of the projectile. Errors in the shock pressure determination result from errors in the impact velocity measurement. Reflections from edge effects from the flyer will be slightly greater in the Wilson schist specimens as they are larger (12 mm, as opposed to 3 mm, in diameter). For the schist experiments we assume that the pressure in the specimen is equal to that in the aluminum, as their density and sound speeds are similar.

**Table S5** Impedance match parameters

<i>Material</i>	<i>Uncompressed density</i> (g/cm <sup>3</sup> )	<i>C</i> (km/s)	<i>s</i>	<i>Source</i>
Al-6061	2.703	5.33 (0.04)	1.34 (0.01)	fit to data between 0 and 3.8 km/s $u_p$ (n = 105) (Marsh, 1980)
Al-2024	2.784 (0.008)	5.38 (0.02)	1.27 (0.02)	fit to data between 0 and 1.3 km/s $u_p$ (n = 26) (Marsh, 1980)
Pyrrhotite	4.603 (0.003)	$U_s = 4.543$ (0.005) km/s		low pressure phase (elastic shock) weighted mean (n = 4) (Ahrens, 1979)
Schist	2.7515 (0.0255)	see Al-2024		mean (n = 4) (Table 1.3, main text)

## 8. Hugoniot Elastic Limit

Two shock experiments to determine the Hugoniot Elastic Limit (HEL) of the solid pyrrhotite single-crystal (No. 127037) were conducted in two perpendicular directions, parallel and perpendicular to the easy plane of magnetization (basal plane) at  $\sim 1150$  m/s. Free surface velocities were determined simultaneously on the aluminum driver (1.2 mm thick) and a  $\sim 2$  mm thick pyrrhotite specimen glued to the downrange side of the aluminum, using a Velocity Interferometer System for Any Reflector (Valyn-VISAR, Barker and Hollenbach, 1972). Shock velocity ( $U_s$ ) in the pyrrhotite was determined from the break-out time difference of the VISAR traces on the driver and pyrrhotite sample (not shown). The experiment perpendicular to  $(00l)$  (solid line in Figure II.5) shows a clear two wave structure with a plateau at  $\sim 300$  m/s indicative of the elastic precursor. Based on CTH simulations, the pressure in the first wave (the HEL) is approximately 3.5 GPa, close to the pressure determined using the particle velocity doubling rule ( $\sim 3$  GPa; e.g., Boslough and Asay, 1993, p.32). Note that the peak measured particle velocity is approximately 50 m/s less than that predicted using the impedance match solution (Table S5). Velocity measurements parallel to  $(00l)$  (dashed line) do not show a clear two-wave structure.

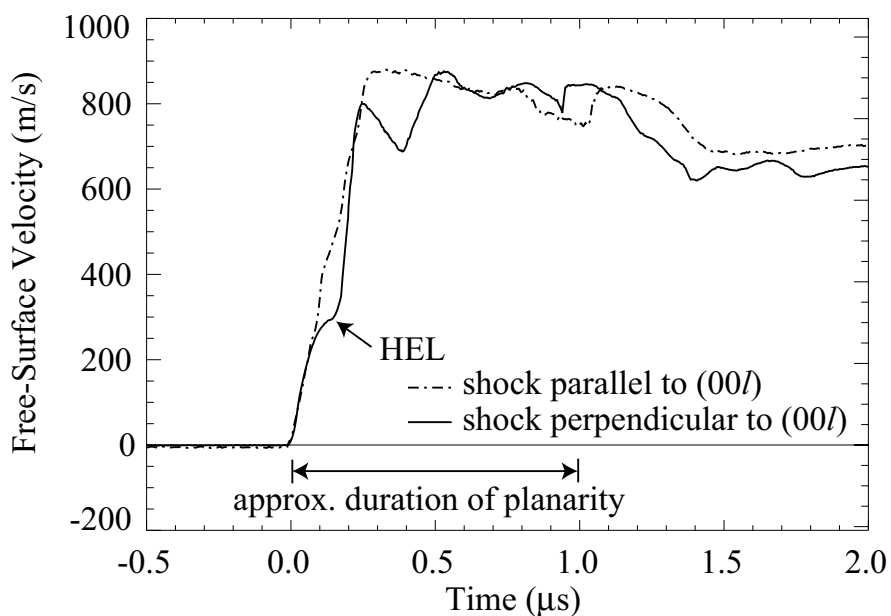


**Figure S5** Free-surface laser velocity interferometry results for pyrrhotite specimens. Solid line = shock direction perpendicular to the basal plane of pyrrhotite  $(00l)$ . Dashed line = shock direction parallel to  $(00l)$ , indicated by \* in other plots and tables throughout the work. HEL = Hugoniot Elastic Limit.

**Table S6** Hugoniot experiment specifics

<i>Specimen Name</i>	<i>Specimen Mass (g)</i>	<i>Specimen thickness (mm)</i>	<i>Specimen density (g/cm<sup>3</sup>)</i>	$c_p$ (m/s)	$c_s$ (m/s)	$\nu$	$v_i$ (m/s)	<i>Tilt (mrad)</i>	$u_p$ (m/s)	$\sigma_I$ (GPa)	$P$ (GPa)	$U_s$ (km/s)	<i>HEL (GPa)</i>
12-C	2.147 (0.0017)	1.9228 (0.0062)	4.5724 (0.0173)	5.034 (0.082)	2.706 (0.025)	0.29	1156 (53.6)	0.36 (0.03)	505 (-24.3/+25.0)	10.8 (-0.53/+0.53)	6.54	-	
12-A*	1.786 (0.0017)	2.0984 (0.0072)	4.6074 (0.0081)	4.887 (0.059)	2.882 (0.021)	0.23	1171 (7.25)	3.77 (6.52)	511 (-2.4/+3.0)	10.9 (-0.08/+0.07)	5.80	4.81 (0.33)	~3.5

$c_p$  and  $c_s$  = longitudinal and shear wave speeds.  $\nu$  = Poisson's ratio.  $v_i$  = measured impact velocity.  $U_s$  = measured shock velocity. *HEL* = Hugoniot Elastic Limit.  $u_p$  = calculated particle velocity.  $\sigma_I$  = calculated principal stress.  $P$  = calculated average pressure.

### 9. Photomicrographs of shocked pyrrhotite

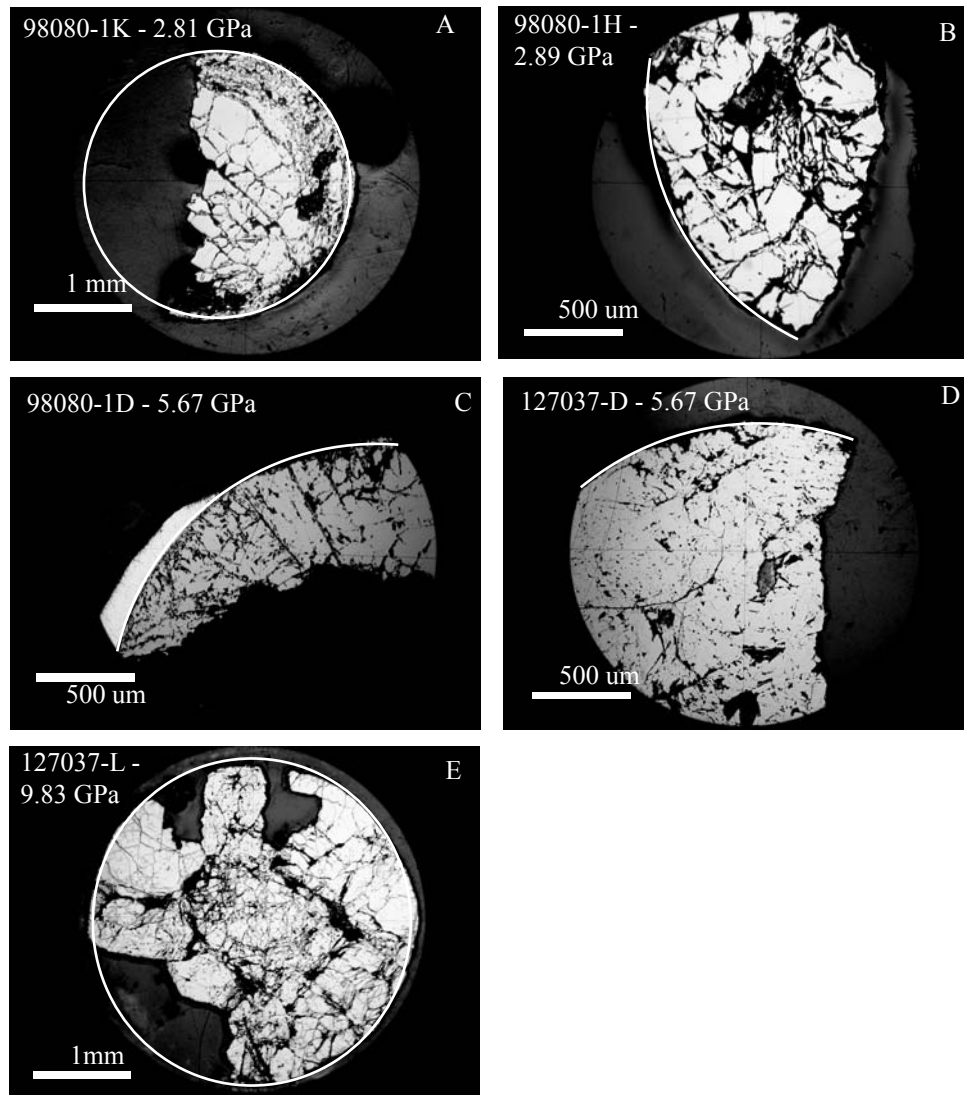


**Figure S6** Photomicrographs of shocked and recovered pyrrhotite nodule (A-C) and single crystal (D and E) specimens. The white line indicates the original perimeter of the disc shaped specimen. The pressures in these samples were near enough to or above the Hugoniot Elastic Limit of pyrrhotite ( $\sim 3$  GPa) that fracturing may have occurred during compression. The nodule specimen shocked at 1.74-1.96 (with uncertain pressure history) and one of the single-crystal specimens shocked at 0.99 GPa samples were also broken when removed from their capsule. In these samples, tensile stresses may have exceeded the dynamic tensile strength of pyrrhotite ( $\sim 100$ s of MPa in igneous rock, Ai and Ahrens, 2004) during release due to the fact that the wave front is not a perfect step function.

## 10. Domain interactions

Domain interference analyses of unshocked and shocked pyrrhotite are shown in Figure S7. Purely noninteracting single-domain assemblages with uniaxial anisotropy are theorized to have a slope of -2 in a  $M_{\text{IRM}}(H)$  versus  $M_{\text{DC}}(H)$  plot (Wohlfarth, 1958), where  $M_{\text{IRM}}(H)$  and  $M_{\text{DC}}(H)$  are the normalized magnetic moments measuring during acquisition of isothermal remanent magnetization and DC backfield demagnetization of saturation isothermal remanent magnetization, in a field,  $H$ , respectively. Deviation from the idealized noninteracting case can be described by the differential remanence,  $\Delta M(H) = M_{\text{DC}}(H) - (1 - 2M_{\text{IRM}}(H))$ . Negative  $\Delta M$  values result from negative interaction yielding a net demagnetizing effect (as is the case in multidomain grains) and positive  $\Delta M$  values result from positive interactions, leading to stabilization of the magnetization.

If domain-size reduction is indeed the cause of magnetic hardening, then the new domains must not interact significantly. Purely noninteracting single-domain assemblages with uniaxial anisotropy are theorized to have a slope of -2 in a  $M_{\text{IRM}}(H)$  versus  $M_{\text{DC}}(H)$  plot (Wohlfarth, 1958), where  $M_{\text{IRM}}(H)$  and  $M_{\text{DC}}(H)$  are the normalized magnetic moments measured during acquisition of isothermal remanent magnetization and DC backfield demagnetization of saturation isothermal remanent magnetization, in a field,  $H$ , respectively (Figure S7A). In the unshocked and postshock (5.67 GPa) SD/SP nodule this slope is -2.14 and -2.13, respectively (Figure S7B), indicating nearly purely noninteracting single-domains and consistent with the uniaxial magnetic anisotropy (linear magnetic fabric) of the nodule. Deviation from the idealized noninteracting case can be described by the differential remanence,  $\Delta M(H) = M_{\text{DC}}(H) - [1 - 2M_{\text{IRM}}(H)]$ . Negative  $\Delta M$  values result from interactions yielding a net demagnetizing effect (as is the case in multidomain grains); positive  $\Delta M$  values result from interactions leading to stabilization of the magnetization. In the MD single-crystal, the differential remanence is negative for all fields, as expected (Figure S7C). The minimum differential remanence at low-field is less in the postshock (9.83 GPa) case than it is in the unshocked case. Comparisons with the observations in Figure 3 of Wehland et al. (2005) indicate that the changes are consistent with a decrease in grain size (a decrease in the net demagnetizing effect), but that the interactions are still of multidomain type.

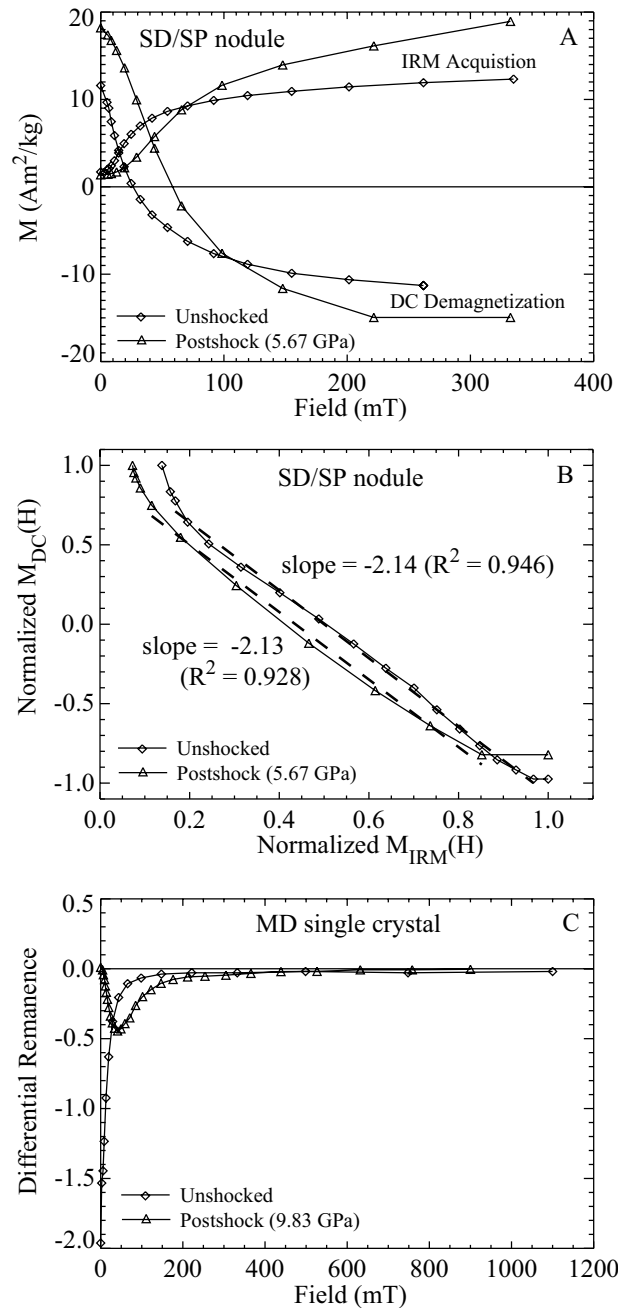


**Figure S7** (A) Isothermal remanence acquisition and (reflected in vertical axis) DC demagnetization of saturation isothermal remanence of unshocked (diamonds) and shocked (5.67 GPa, triangles) SD/SP pyrrhotite nodule. (B) Normalized acquisition and DC demagnetization intensities of saturation isothermal remanence at the same field values from panel A. Thick dashed lines are linear fits to portions of the data. (C) Differential remanence,  $\Delta M(H) = M_{\text{DC}}(H) - (1 - 2M_{\text{IRM}}(H))$  of unshocked (diamonds) and shocked (9.83 GPa) triangles MD single crystal pyrrhotite. Negative  $\Delta M$  values indicated multidomain type interactions.

## 11. Magnetic imaging of the pyrrhotite nodule

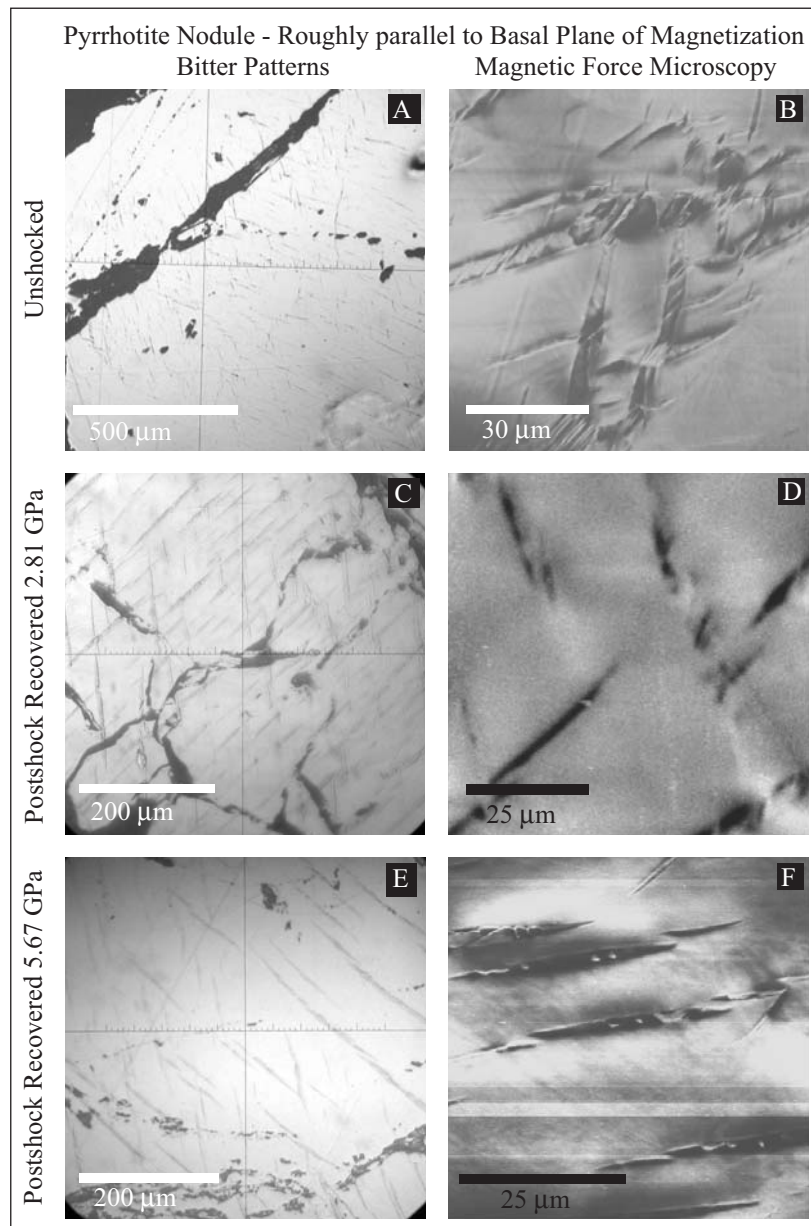


**Figure S8** Magnetic imaging of polished ( $0.02\ \mu\text{m}$ ) (**A, B**) unshocked and (**C-F**) postshock recovered SD/SP pyrrhotite, with the shock direction roughly parallel to the basal plane in all. Postshock samples are AF demagnetized in 85 mT peak fields. Horizontal lines in (**F**) are an artifact of tracking error.

## 12. References

- Ahrens, T.J., 1979. Equations of State of Iron Sulfide and Constraints on the Sulfur Content of the Earth. *JGR* 84, 985-998.
- Ai, H.-A. and T.J. Ahrens, 2004. Dynamic tensile strength of terrestrial rocks and application to impact cratering. *MAPS* 39 (2), 233-246.
- Barker, L.M. and R.E. Hollenbach, 1972. Laser interferometer for measuring high velocities of any reflecting surface. *Journal of Applied Physics* 43, 4669-4675.
- Boslough, M.B. and J.R. Asay, 1993. Chapter 2: Basic Principles of Shock Compression, in: Asay, J.R. and S. M. (Eds), *High-Pressure Shock Compression of Solids*. Springer-Verlag, New York, pp. 7-42.
- Coe, R.S., 1966. Analysis of Magnetic Shape Anisotropy Using Second-Rank Tensors. *JGR* 71 (10), 2637-2644.
- Dekkers, M.J., 1988. Magnetic properties of natural pyrrhotite Part I: Behaviour of initial susceptibility and saturation-magnetization-related rock-magnetic parameters in a grain-size dependent framework. *PEPI* 52, 376-393.
- Dekkers, M.J., J.L. Mattei, G. Fillion and P. Rochette, 1989. Grain-Size Dependence of the Magnetic-Behavior of Pyrrhotite During Its Low-Temperature Transition at 34-K. *GRL* 16, 855-858.
- Gattacceca, J., A. Lamali, P. Rochette, M. Boustie and L. Berthe, 2007. The effects of explosive-driven shocks on the natural remanent magnetization and the magnetic properties of rocks. *PEPI* 162, 85-98, doi:10.1016/j.pepi.2007.1003.1006.
- Jelínek, V., 1973. Precision A.C. bridge set for measuring magnetic susceptibility of rocks and its anisotropy. *Studia Geophysica & Geodaetica* 17, 36-48, doi:10.1007/BF01614027.
- Jelínek, V., 1981. Characterization of the magnetic fabric of rocks. *Tectonophysics* 79, T63-T67, doi:10.1016/0040-1951(81)90110-4.
- Marsh, S.P., (Ed) *LASL Shock Hugoniot Data*, University of California Press, Berkeley, California, 1980, 658 pp.
- Martín-Hernández, F., M.J. Dekkers, I.M.A. Bominaar-Silkens and J.C. Maan, 2008. Magnetic anisotropy behaviour of pyrrhotite as determined by low-and high-field experiments. *GJI* 174, 42-54, doi: 10.1111/j.1365-246X.2008.03793.x.
- McGlaun, J.M., S.L. Thompson and M.G. Elrick, 1990. CTH: A 3-dimensional shock-wave physics code. *Int. J. Impact Eng.* 10, 351-360, doi:10.1016/0734-743X(90)90071-3.
- Melosh, H.J., 1989. *Impact Cratering: A Geologic Process*, Oxford University Press, New York.

- Nkoma, J.S. and G. Ekosse, 1999. X-ray diffraction of chalcopyrite  $\text{CuFeS}_2$ , pentlandite  $(\text{Fe,Ni})_9\text{S}_8$  and pyrrhotite  $\text{Fe}_{1-x}\text{S}$  obtained from Cu-Ni ore bodies. *Journal of Physics: Condensed Matter* 11, 121-128.
- Rochette, P., J.-L. Mattéi and M.J. Dekkers, 1990. Magnetic transition at 30-34 Kelvin in pyrrhotite: insight into a widespread occurrence of this mineral in rocks. *EPSL* 98, 319-328.
- Wehland, F., A. Stancu, P. Rochette, M.J. Dekkers and E. Appel, 2005. Experimental evaluation of magnetic interaction in pyrrhotite bearing samples. *PEPI* 153, 181-190, doi:10.1016/j.pepi.2005.05.006.
- Wohlfarth, E.P., 1958. Relations between different modes of the acquisition of the remanent magnetization of ferromagnetic particles. *Journal of Applied Physics* 29, 595-596.